ORIGINAL RESEARCH ARTICLE

Effect of Strong transient Variations in Operational Parameters on Vacuum Arc Remelting (VAR)

M. ABDI, E. KARIMI-SIBAKI, M. WU, and A. KHARICHA

Numerical simulations are employed to investigate the impact of strong transient variations in electrode diameter and melt rate on ingot growth in the vacuum arc remelting process of alloy 718. As the electrode diameter changes, side arcing and arc distribution are also affected, significantly influencing pool depth throughout transient ingot growth. To evaluate these effects, a parametric study is conducted to analyze potential variations in side arcing and arc distribution during the process. The findings reveal that electromagnetic forces play a dominant role in shaping the melt pool. A slight increase in side arcing results in a shallower melt pool, while a higher arc ratio (more diffusive arc) further reduces pool depth, increasing the influence of thermal buoyancy forces. Additionally, smaller electrode diameters and higher melt rates contribute to a deeper pool profile. The simulation results align with the experimental data, confirming the accuracy and reliability of the model.

https://doi.org/10.1007/s11663-025-03749-8

I. INTRODUCTION

VACUUM arc remelting (VAR) is a metallurgical process designed to produce ingots with exceptional chemical uniformity and minimal impurities. By operating in a vacuum, VAR effectively prevents oxidation, ensuring a high-purity melt. This process also facilitates the removal of low-density oxide inclusions and the evaporation of undesirable elements with high vapor pressures, such as lead (Pb), tin (Sn), bismuth (Bi), and manganese (Mn). These elements can condense on the mold wall, promoting crown formation and influencing both electric current flow and heat distribution. In VAR, a consumable electrode is melted under vacuum using a direct current (DC) electric arc. The molten metal droplets then fall into a water-cooled copper crucible. The intense heat generated by the electric arc, along with the continuous addition of molten droplets and the cooling effect of the water-cooled mold, sustains a persistent hemispherical molten region,[1] as known as melt pool, at the top of the ingot throughout the remelting process, as shown schematically in Figure 1(a). This process is extensively used in industry for producing alloys such as titanium and zirconium alloys, nickel-based alloys, and steels.[2,3]

Understanding the VAR process involves exploring a complex interplay of factors that influence the quality and uniformity of the ingots. Central to this process are the cathode spots,[4–7] where electric arcs[8–10] initiate and metal transfer occurs. The electric arc, sustained between the electrode tip (cathode) and the top of the ingot (anode), is the primary source of thermal energy essential for remelting the consumable electrode. The distribution and stability of cathode spots are critical, as they determine the arc's behavior within the vacuum region,[9] profoundly influencing energy transfer to the ingot's surface and shaping the resulting melt pool dynamics. The arc's distribution, shaped by the pattern of cathode spots,[10,11] can lead to various arc modes, including diffuse, diffuse columnar, and multiple arcs,[10,12] each with distinct effects on the thermal gradients and fluid flow within the molten pool.

Another phenomenon that impacts the molten pool is solidification shrinkage. Solidification shrinkage occurs when the molten metal cools and solidifies, resulting in a reduction in volume. This volumetric contraction creates gaps between the solidifying metal and the mold, causing the ingot to lose direct contact with the mold surface. Consequently, heat transfer shifts from conduction, efficient when in contact, to radiation, which is much less effective.[13] This shift can significantly impact the cooling rate and overall solidification process,

M. ABDI and M. WU are with the Chair for Modeling and Simulation of Metallurgical Processes, Department of Metallurgy, Montanuniversitaet, Franz-Josef Street 18, 8700 Leoben, Austria. Contact e-mail: mehran.abdi@unileoben.ac.at E. KARIMI-SIBAKI and A. KHARICHA are with the Chair for Modeling and Simulation of Metallurgical Processes, Department of Metallurgy, Montanuniversitaet and also with the Christian Doppler Laboratory for Metallurgical Applications of Magnetohydrodynamics, Franz-Josef Street 18, 8700 Leoben, Austria. Contact e-mail: abdellah.kharicha@unileoben.ac.at

Manuscript submitted March 24, 2025; accepted August 4, 2025.

Published online: 21 August 2025

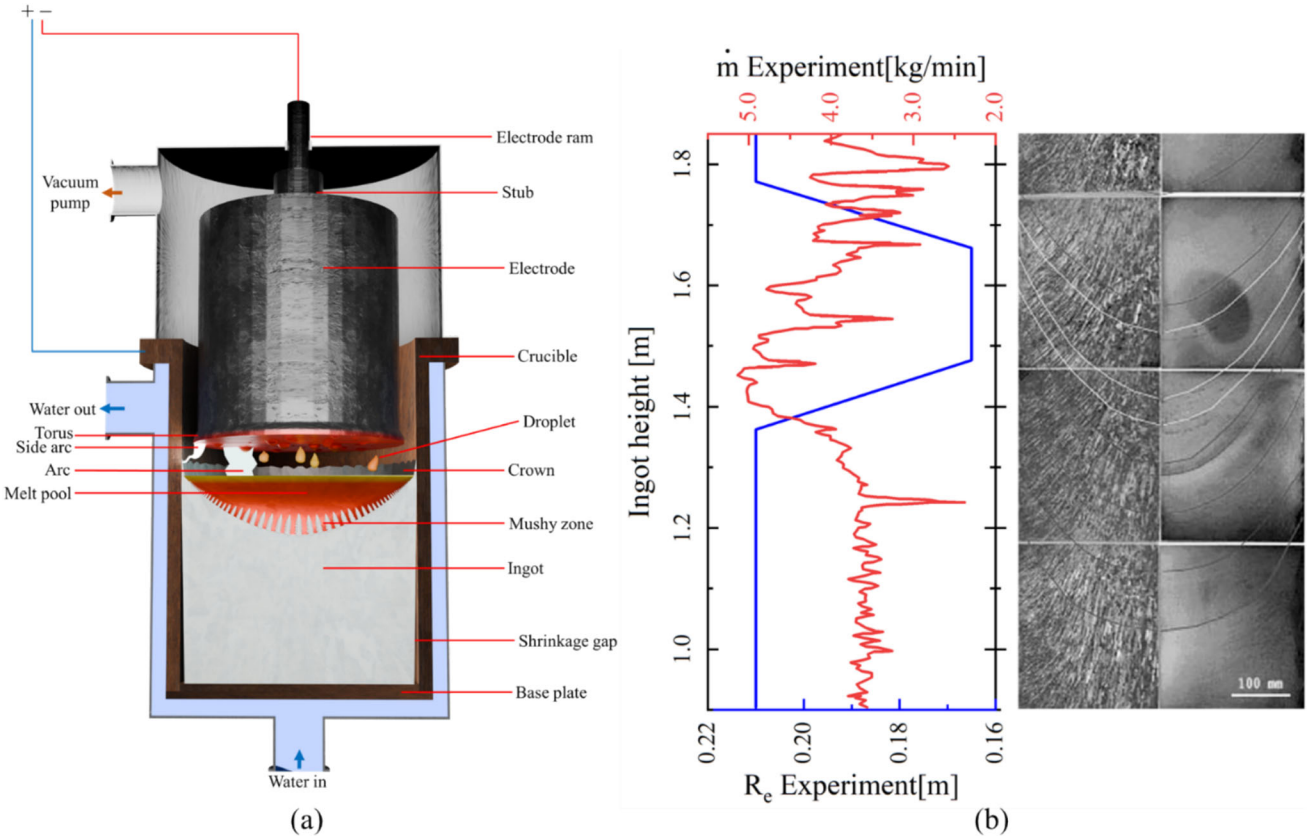

Fig. 1—(*a*) Schematic representation of the VAR process, illustrating its primary physical phenomena and components. (*b*) Left) Electrode radius (R_e) used and the melt rate ($\dot{m}$) in the experiment by Wang *et al.*,[19] (b) Right) Experimental pool profiles from Wang *et al.* (Metallurgical and Materials Transactions A).[19]

potentially deepening the molten pool and ultimately reducing the quality of the metal. To address these challenges, gas cooling is employed.[14] Gas cooling regulates the cooling rate by providing controlled and uniform cooling to the ingot surface. This method enhances heat transfer efficiency by compensating for the reduced conduction and helps maintain a more stable temperature gradient, resulting in a more consistent solidification process and improved metal quality. Hosamani *et al.*[15] investigated the effects of gas cooling and the impact of cooling gas pressure through experiments, while Karimi-Sibaki *et al.*[16] confirmed the above-mentioned findings via simulations. Moreover, a coupled thermal stress–strain and MHD model developed by Bohacek *et al.*[17] demonstrated that the size and position of the shrinkage gap are directly influenced by the temperature distribution and the mechanical response of the ingot.

The melt rate is another important factor in the vacuum arc remelting (VAR) process. Sankar *et al.*[18] investigated the effects of melt rate variations, discovering that a lower melt rate produced a more favorable grain structure characterized by nearly parallel columnar grains, whereas a higher melt rate led to a deeper molten pool and inclined grain orientation. Additionally, increased melt rates have been linked to the formation of defects, including freckles and solidification white spots.[19–22] Kermanpur *et al.*[23] further explored the impact of varying melt rate and arc power on grain structure. They discovered that higher melt rates refined the grain structure, while varying arc voltage impacted the chill zone (adjacent to mold) and grain morphology. Building on control challenges, Williamson *et al.*[24,25] developed a new model-based melt rate controller that managed disturbances like transverse cracks in the electrode effectively. Despite its success, solidification white spots persisted, suggesting that maintaining a constant melt rate is more effective than controlling current for minimizing crack impacts. Cui *et al.*[26] examined the effect of melting rate on grain structure, finding that higher melting rates lead to finer grains.

The electrode diameter plays a crucial role in VAR, affecting both thermal and electrical current distribution, which in turn impacts ingot quality. Delzant *et al.*[27] pointed out that a larger electrode radius expands the low-radiation zone beneath it, affecting the thermal profile. Jiang *et al.*[28] highlight that a smaller diameter raises current density, enhancing melting and promoting a more uniform inclusion distribution, while a larger diameter may reduce melting efficiency. Additionally, Wang *et al.*[19] studied how variations in electrode diameter and arc gap during ingot growth impacted freckle formation in INCONEL® 718, finding that substantial changes in these parameters disrupted fluid flow and led to freckle defects and solidification

instability. In their experiment, the electrode diameter changed from 420 to 320mm, then back to 420mm, forming a trapezoidal profile. As the electrode diameter began to change while maintaining a constant electric current, the melt rate exhibited greater fluctuations, as shown alongside the electrode diameter variation in Figure 1(b). These changes in electrode diameter and fluctuation in melt rate caused the melt pool depth to alternate between thicker and thinner, as well as deeper and shallower pool profiles. This behavior is also evident in the cut ingot with extracted pool profiles, corresponding to the recorded melt rate and electrode diameter, as illustrated in Figure 1(b).

The underlying cause of these melt pool variations lies in the effects of arc distribution and side arcing, which directly influence the solidification process. To better understand these effects, a fully transient numerical model is employed to investigate how variations in melt rate and electrode diameter affect pool depth during ingot growth in the vacuum arc remelting (VAR) process, from the ingot base (start) to its final height (feeding). As these parameters dynamically change, a parametric study is conducted to examine the influence of arc distribution and side arcing under transient conditions, as well as their impact on solidification behavior in the VAR process. Although the present parametric study varies arc ratio and side arcing independently to explore their influence on melt pool behavior, these variations are examined under the transient conditions of melt rate and electrode diameter derived from the experimental case.

II. MODELING

The symbols used for modeling are listed in "Nomenclature." The numerical model was developed by the authors within the ANSYS Fluent environment,[29] incorporating user-defined functions (UDFs) to capture the specific features of the VAR process, including electromagnetic field calculation, solidification, source terms, boundary conditions, and process-specific features, such as the arc distribution and side arcing effects. The schematic of the vacuum arc remelting (VAR) setup, shown in Figure 1(a), summarizes the phenomena regarding the remelting and solidification of an alloy in VAR. The electrode, with a varying diameter of max. 420mm and min. 330mm, melts inside the 508mm ingot. The following assumptions were made for the simulations:

I. Although the entire process is inherently three-dimensional, due to the cylindrical growth of the ingot and the dominance of the magnetic field in the azimuthal direction, a 2D axisymmetric model is assumed.
II. A portion of the current enters the ingot from the mold, while the remainder returns to the electrode without contacting the ingot, as side arcing.[16,30] The magnitude of side arcing is specified, and various values are examined.
III. The calculations focus on the ingot applying adequate boundary conditions, excluding the mold, electrode, and plasma.
IV. The electromagnetic field is determined as a one-way coupling where thermal and flow fields do not influence the electromagnetic field.[16]
V. The top of the ingot remains flat and undisturbed.
VI. The Marangoni effect is neglected because it is significantly weaker than thermal buoyancy forces in the VAR process and has minimal impact on melt pool flow.[31]
VII. Solutal buoyancy is neglected because melt pool dynamics are dominated by electro-vortex and thermal buoyancy flows, rendering the effect of composition-driven buoyancy forces negligible.[32]
VIII. Joule heating is neglected because the arc is the dominant heat source in VAR, and the heat generated within the ingot by electric current flow is comparatively minimal (See Section III-C).[33]
IX. The impact of droplets on the ingot top is approximated by a uniform mass flow rate.
X. The size of the mold–ingot interface boundary remains constant, and the shrinkage gap is not calculated explicitly.
XI. Arc gap evolution is not modeled.

A. *Governing Equation*

All governing equations, Eqs. [1] through [17], related to the electromagnetic, thermal and solidification, and flow fields in cylindrical coordinates are listed in Table I.

The electric field was determined through the calculation of the electric scalar potential, ϕ, according to the Laplace equation, Eq. [1].

Ohm's Law, Eqs. [2] and [3], and Ampere's Law, Eq. [4], were utilized to determine the electric current density (J_z, J_r) and the magnetic field (B_θ), respectively.

By utilizing the electric current density (J_z and J_r) and the tangential magnetic field (B_θ), the Lorentz force (F_z and F_r) were computed through Eqs. [5] and [6].

The electric potential at the ingot–mold interface and the base plate, where the contact between the ingot and mold persists, is set to zero. Conversely, in the shrinkage gap, where the ingot no longer maintains contact with the mold, the electric potential flux is set to zero. Following the work of previous researchers,[16,21,34–39] the Gaussian distribution of electric current density ($J = \frac{I_0(1-f_{side-arc})exp(-\frac{r^2}{R_a{}^2})}{\int_0^{R_i} 2\pi r exp(-\frac{r^2}{R_a{}^2})dr}$), where $R_a = f_R R_i$, is applied to the ingot's top surface.

The arc ratio (f_R) describes the radial extent of the electric arc on the ingot top surface relative to the ingot radius. For example, an arc ratio of 70 pct implies that the arc covers 70 pct of the ingot radius (R_i), resulting in a more diffuse energy distribution. Conversely, a lower arc ratio indicates that the arc is concentrated in a narrower region near the ingot center, leading to a more intense and focused heat input.

To determine the temperature distribution within the ingot, the conservation of enthalpy, Eqs. [7] and [8], must be satisfied. The Gulliver-Scheil model,[40] widely applied to simulate the solidification of nickel-based superalloys,[41] was used to estimate the solidification path, Eqs. [9] and [10]. Heat transfer at the ingot–mold interface and the baseplate–ingot interface is specified with a heat transfer coefficient (HTC) of $500.0\mathrm{W\,m^{-2}K^{-1}}$. In the shrinkage gap, where the ingot does not contact the mold, helium gas is injected, and the same HTC value of $500.0\mathrm{Wm^{-2}K^{-1}}$ is assumed.[13]

The heat transfer at the top of the ingot involves the complex arc moving above the ingot and the contribution from droplets of hot metal, which are approximately 100.0 to 200.0 °C higher than the liquidus temperature.[42] To account for these factors, the empirical equation $T = \begin{cases} T_l + \Delta T(I, R_i), r < R_e \\ T_l + \Delta T(I, R_i)\frac{R_m - r}{R_m - R_e}, r \geq R_e \end{cases}$, where $\Delta T(I, R_i) = 400e^{-\frac{24R_i}{I}}$, proposed by Kondrashov *et al.*,[43,44] was applied to include the distribution of electric current at the ingot top.

To describe the flow field in the melt pool and the mushy zone, the incompressible form of the Navier--Stokes equations was utilized. To satisfy mass conservation, the continuity equation, Eq. [11], was solved, along with two momentum equations, Eqs. [12] and [13], for the flow components in the radial and axial directions (u_z, u_r). S_{u_z} and S_{u_r} in the momentum equations are source terms providing body forces in the z and r directions, respectively, given by Eqs. [14] and [15]. The definitions of the different parts of the source terms (S_{u_z} and S_{u_r}) are as follows:

The interdendritic flow inside the mushy zone is modeled according to Darcy's Law, Eqs. [16] and [17], incorporating the momentum source $\left(-\left(\frac{\mu_{eff}}{\kappa}\right)u_z\right.$ and $\left.-\left(\frac{\mu_{eff}}{\kappa}\right)u_r,\right)$ due to the reduced porosity in the mushy zone, following the approach of Schneider *et al.*.[45] The isotropic model of Carman-Kozeny[46] is utilized to estimate the drag resistance of dendrites against the flow in the mushy zone.[38,46,47] Additionally, the Boussinesq approximation was used to model the buoyancy force $\left(g\rho\beta\frac{h-h_{ref}}{C_p}\right)$, and, as defined previously, the Lorentz forces with axial and radial components are also included. The SST k-ω turbulence model was used to capture the effects of turbulence. This model is effective in predicting flow separation and adverse pressure gradients, making it suitable for complex flow simulations. It combines the advantages of both the k-ε and k-ω models, providing a robust approach for simulating turbulent flows. The SST k-ω model is particularly effective for near-wall treatment and is less sensitive to grid spacing. It offers accuracy comparable to the LES model with lower computational cost. Detailed information about this model can be found in the Ref. 48.

The boundary conditions for flow involve droplets falling into the pool directly beneath the electrode, leading to a non-zero mass flow rate ($\dot{m}$) in this area. Conversely, the mass flow rate is zero away from the electrode: $\left(\dot{m} = \begin{cases} \rho\pi {R_e}^2 u_z, r < R_e \\ u_z = \frac{\partial u_r}{\partial r} = 0, r \geq R_e \end{cases}\right)$.

A no-slip boundary condition is applied to all other boundaries. The layering method was used for the dynamic mesh,[29] aiming to model transient ingot growth. The base plate remains steady, while the axis, shrinkage gap, ingot–mold interface, and ingot top move upward with the speed of $u_{mesh} = \frac{\dot{m}}{\rho \cdot \pi \cdot {R_i}^2}$ where R_i is the Radius of the ingot. The criteria for adding a new layer of structured mesh to the top of the ingot is: $h_{mesh} \geq (1 + \alpha_c)h_{ideal}$. The height ($h_{mesh}$) of the last layer, adjusted to the ingot top, is extended until it exceeds $(1 + \alpha_c)h_{ideal})$, where α_c is 0.4. Notably, the high-quality quadrilateral mesh elements are preserved.

B. *Other Settings*

Remelting was performed under a constant helium gas pressure of approximately 0.5kPa in the mold. Material properties extracted from literature.[39,49–54] The operational conditions were adapted from Wang *et al.*[19] Both the material properties and operational conditions are summarized in Table II. Temperature-dependent material properties listed in Table II are implemented using piecewise linear interpolation between the tabulated values.

Figure 2(a) provides a detailed view of the proposed 2D axisymmetric cross-section, highlighting the ingot region and boundaries. The left-hand side of Figure 2(a) shows the schematic of the mold at t_0 (the beginning of the simulation), while the right-hand side illustrates schematically the stage of the model at t_1 (the end of the simulation).

Side arcing has been reported to account for 15 to 70 pct of the total current in VAR, according to the review by Risacher *et al.*[55] Arc distribution is another critical factor and can be evaluated using magnetic sensors,[36,56–62] optical imaging,[60,63–65] or high-speed cameras to track arc position and movement.[12,64,66–69] In this study, side arcing is assumed to be 25 and 30 pct of the total current,[16,34] and the arc radius ranges from 65 to 70 pct of the ingot radius. The effects of both parameters are illustrated by the Gaussian current distribution at the top of the ingot in Figure 2(b).

C. *Computational Procedure*

The Finite Volume Method (FVM) was employed to discretize the governing equations within the computational domain. Discretization techniques included Least Squares Cell-Based for gradient calculations, PRESTO! for pressure calculations, Second-Order Upwind for momentum, turbulent kinetic energy, specific dissipation rate, energy, and electric potential equations. Pressure–velocity coupling was achieved through the SIMPLEC scheme. All simulations were conducted transiently with a small time-step of 0.1 s to ensure convergence.

Table I. Governing Equations of Electromagnetic, Thermal and Solidification, and Flow Fields

Electromagnetic Field

$$\frac{\partial}{\partial z}\left(\sigma_e \frac{\partial \phi}{\partial z}\right) + \frac{1}{r}\frac{\partial}{\partial r}\left(r\sigma_e \frac{\partial \phi}{\partial z}\right) = 0 \quad [1]$$

$$J_z = -\sigma_e \frac{\partial \phi}{\partial z} \quad [2]$$

$$J_r = -\sigma_e \frac{\partial \phi}{\partial r} \quad [3]$$

$$B_\theta = \mu_m \frac{1}{r}\int_0^r J_z dr \quad [4]$$

$$F_z = J_r \cdot B_\theta \quad [5]$$

$$F_r = -J_z \cdot B_\theta \quad [6]$$

Solidification and Thermal Field

$$\frac{\partial}{\partial t}(\rho h) + \frac{\partial}{\partial z}(\rho u_z h) + \frac{1}{r}\frac{\partial}{\partial r}(\rho r u_r h) = \frac{\partial}{\partial z}\left(\frac{k_{eff}}{C_p}\frac{\partial h}{\partial z}\right) + \frac{1}{r}\frac{\partial}{\partial r}\left(r\frac{k_{eff}}{C_p}\frac{\partial h}{\partial z}\right) + S_h \quad [7]$$

$$S_h = -\frac{\partial}{\partial t}(\rho f_l L) - \frac{\partial}{\partial z}(\rho u_z f_l L) - \frac{1}{r}\frac{\partial}{\partial r}(\rho r u_r f_l L) \quad [8]$$

$$f_l = \begin{cases} 1, T > T_l \\ 1 - \left(\frac{T_m - T}{T_m - T_l}\right)^{\frac{1}{k-1}}, T_s < T < T_l \\ 0, T < T_s \end{cases} \quad [9]$$

$$T_m = m_l \cdot C_0 + T_l \quad [10]$$

Flow Field

$$\frac{\partial}{\partial t}(\rho) + \frac{\partial}{\partial z}(\rho u_z) + \frac{1}{r}\frac{\partial}{\partial r}(\rho r u_r) = 0 \quad [11]$$

$$\frac{\partial}{\partial t}(\rho u_z) + \frac{\partial}{\partial r}(\rho u_r u_z) + \frac{\partial}{\partial z}(\rho u_z u_z) = -\frac{\partial}{\partial z}(p) + \mu_{eff}\left[\frac{1}{r}\frac{\partial}{\partial r}\left(r\frac{\partial}{\partial r}(u_z)\right) + \frac{\partial^2}{\partial z^2}(u_z)\right] + S_{u_z} \quad [12]$$

$$\frac{\partial}{\partial t}(\rho u_r) + \frac{\partial}{\partial r}(\rho u_r u_r) + \frac{\partial}{\partial z}(\rho u_z u_r) = -\frac{\partial}{\partial r}(p) + \mu_{eff}\left[\frac{\partial}{\partial r}\left(\frac{1}{r}\frac{\partial}{\partial r}(r u_r)\right) + \frac{\partial^2}{\partial z^2}(u_r)\right] + S_{u_r} \quad [13]$$

$$S_{u_z} = -\left(\frac{\mu_{eff}}{\kappa}\right)u_z + F_z - g\rho\beta\frac{h - h_{ref}}{C_p} \quad [14]$$

$$S_{u_r} = -\left(\frac{\mu_{eff}}{\kappa}\right)u_r + F_r \quad [15]$$

$$\frac{\mu}{\kappa} = A_{mush}\frac{(1-f_l)^2}{f_l^3} \quad [16]$$

$$A_{mush} = 1.66 \times 10^3 \frac{\mu}{\lambda_1^2} \quad [17]$$

III. RESULTS AND DISCUSSIONS

This section presents the simulation results together with experimental comparisons and corresponding interpretations. The results are first introduced through a general overview of field evolution during transient ingot growth, followed by detailed parametric studies on side arcing and arc distribution. This combined presentation is intended to offer a comprehensive understanding of how transient variations in melt rate, electrode diameter, and arc behavior influence melt pool dynamics and solidification behavior in the VAR process.

Herein, the numerical model is used to examine field structures during transient ingot growth, specifically under conditions with 30 pct side arcing and a 70 pct arc ratio. Figure 3 shows simulation results for a side arcing of 30 pct and an arc ratio of 70 pct. Snapshots are provided at four distinct heights of the ingot: (a) 300, (b) 800, (c) 1300, and (d) 1800mm. The results encompass current density, magnetic field, Lorentz force, temperature, velocity, and liquid fraction (from left to right), including isolines of liquid fractions of 0.97 and 0.06. The current intensity is higher at the top of the ingot due to the distribution of the arc (Gaussian distribution) and the current entering through the ingot–mold interface, resulting in stronger magnetic fields. As a result of the interaction between the magnetic field and the electric current, the Lorentz force is also stronger at the top, acting from the ingot's outer surface toward its axis. The high temperature at the top of the ingot, due to the distribution of the arc and the elevated temperature of the droplets entering the ingot melt pool, along with significant cooling from the sides, results in the formation of a hemispherical-shaped pool. The Lorentz force and thermal buoyancy mix the liquid effectively in the pool, creating a relatively uniform temperature distribution. Initially, when the ingot is shorter, cooling from the base leads to a shallower pool. As the ingot height increases, the effect of base cooling diminishes, causing the pool to become deeper.[13] Additionally, the shrinking gap is filled with helium gas, enhancing heat extraction from the ingot and leading to a shallower pool depth compared to scenarios without gas cooling.[15,16]

The velocity exhibits two distinct vortex flows within the pool: one associated with the electro-vortex flow (EVF) and the other with the thermal buoyancy flow (TBF). Throughout the entire ingot height, from the small ingot tail to the higher lengths, the EVF remains dominant in the pool. To observe the transient ingot growth over time, videos of three different cases are provided as supplementary materials. These videos provide a visual representation of the dynamic processes through ingot growth to gain a deeper understanding of how transport phenomena evolve under different conditions.

Table II. Material Properties and Operation Conditions

Material Properties, Symbol, Unit	Value	References
Electric Conductivity, σ_e, $\Omega^{-1}m^{-1}$	7.5×10^5	[54]
The Magnetic Permeability, μ_m, $Jm^{-1}A^{-2}$	$4\pi \times 10^{-7}$	—
Density, ρ, kgm^{-3}	7491.0	[39]
Effective Thermal Conductivity, k_{eff}, $Wkg^{-1}m^{-1}$	(293.0*K*, 11.4), (373.0*K*, 12.5), (573.0*K*, 14.0), (773.0*K*, 15.5), (973.0*K*, 21.5), (1173.0*K*, 26.2), (1623.0*K*, 31.3), (2500.0*K*, 35.0)	[49]
Heat Capacity, C_p, $Jkg^{-1}K^{-1}$	(293.0*K*, 427.14), (373.0*K*, 441.7), (573.0*K*, 481.7), (773.0*K*, 521.7), (973.0*K*, 561.7), (1173.0*K*, 601.7), (1623.0*K*, 691.7), (2500.0*K*, 700.0)	[49]
Latent Heat of Solidification, L, Jkg^{-1}	272000.0	[39]
Melting Temperature, T_m, K	1661.5	—
Liquidus Temperature, T_l, K	1609.0	[39]
Solidus Temperature, T_s, K	1533.0	[39]
Equilibrium Partition Coefficient, k, –	0.48	[51]
Slope of the Liquidus Line, m_l, k pct^{-1}	10.5	[51]
Initial Solute Concentration, C_0, Wt *Pct*	5.0	[51]
Thermal Expansion, β, K^{-1}	1.3×10^{-5}	[50]
Primary Dendrite Arm Spacing, λ_1, m	7.5×10^{-6}	[52, 53]
Effective Viscosity, μ_{eff}, Pas	5.3×10^{-3}	[50]
Gravitational Acceleration, g, ms^{-2}	9.81	—

Operation Condition, Symbol, Unit	Value	References
Total Imposed Current, I_0, *A*	6000.0	[19]
Radius of Ingot, R_i, m	0.254	[19]
Ingot Height, (min, Max), m	0.25, 1.88	[19]
Radius of Mold, R_m, m	0.279	[19]
Radius of Electrode, R_e, m	variable, see Fig. 4(a)	[19]
Mass Flow Rate, $\dot{m}$, kg min^{-1}	variable, see Fig. 4(a)	[19]

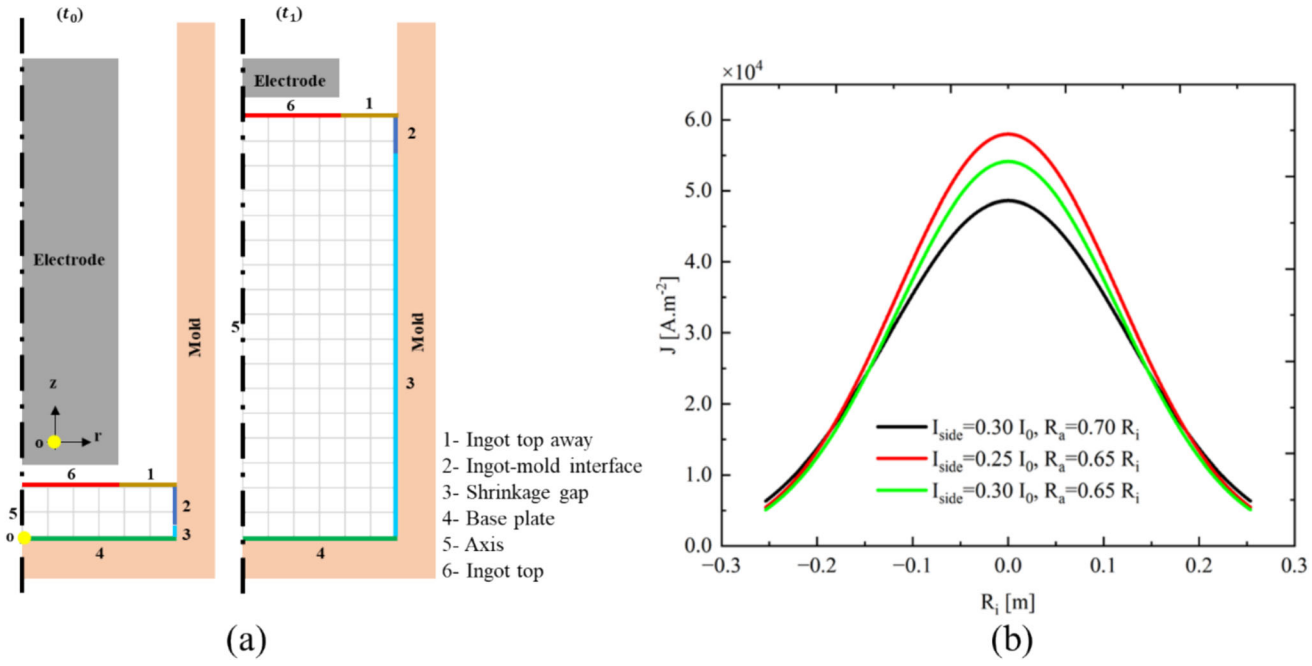

Fig. 2—(*a*) The 2D axisymmetric domain used in the calculation from the base (start stage t_0) to the final height (feeding stage t_1). The grid represents the mesh; for representation purposes, the mesh elements are coarser by a factor of 10 compared to the real simulations. (*b*) Electric current Gaussian distribution at the top of the ingot.

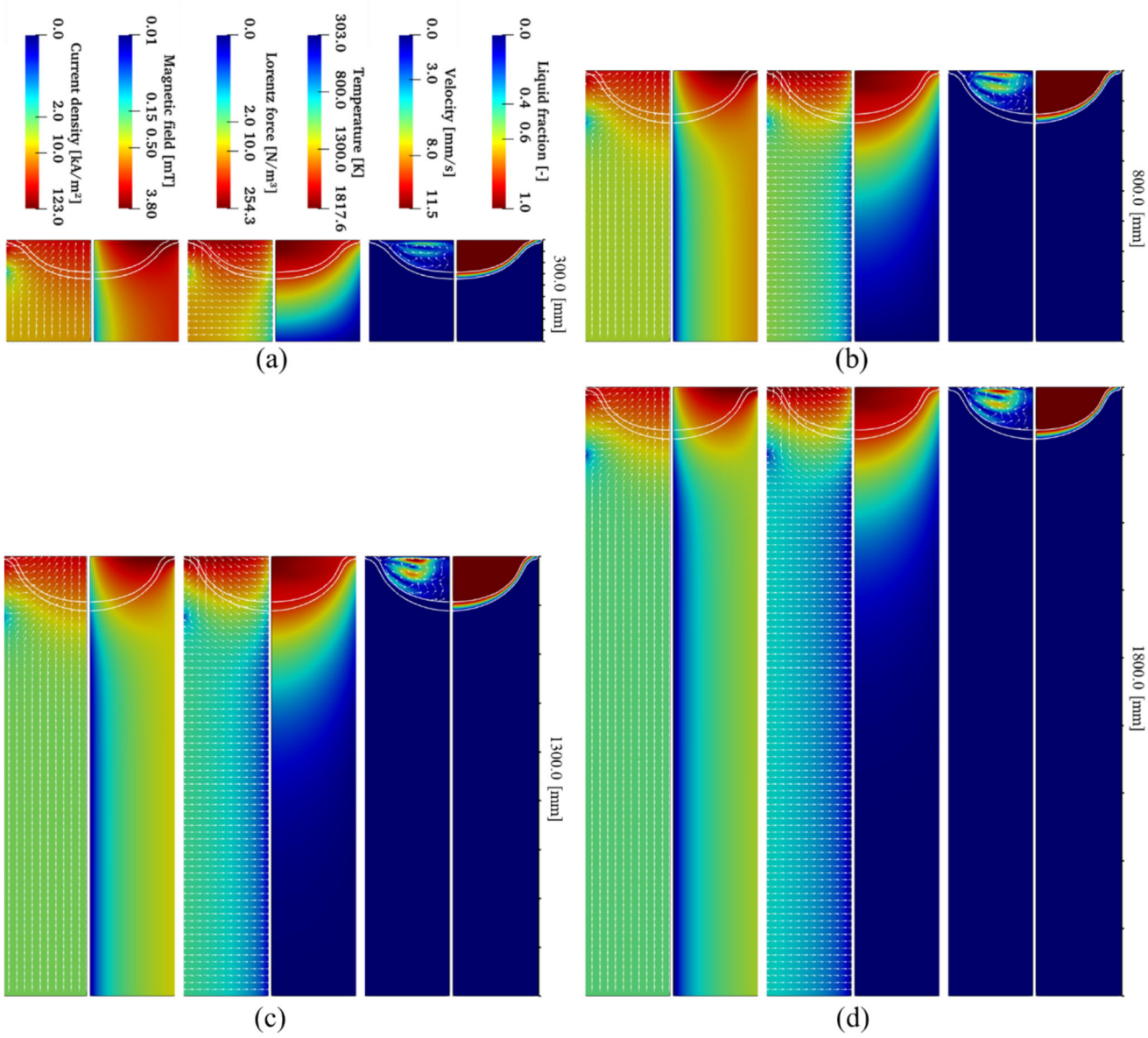

Fig. 3—Simulation results of field distributions, including current density, magnetic field, Lorentz force, temperature, velocity, and liquid fraction, for a side arcing of 30 pct and an arc ratio of 70 pct at different heights. (*a*) 300, (*b*) 800, (*c*) 1300, and (*d*) 1800mm. Isolines denote liquid fractions of 0.97 and 0.06. White vectors indicate field directions.

The proposed model involves two key uncertainties frequently discussed in VAR research: the arc distribution above the ingot top[36,63,67,68] and the amount of side arcing.[16,30,55,56,70,71] These uncertainties arise from the complex behavior of plasma in the vacuum, the dynamic nature of the arc (whether centric, eccentric, diffusive, or constricted), the variations in crown height,[55] the shrinkage gap,[17] and the height of the ingot.

A. *Effects of Side Arcing*

In this study, the electrode geometry follows the experimental design, with a nominal diameter of 420mm. Only for the trapezoidal machined section, we adopt an idealized geometry represented by two reduced sections: from 420 to 370mm, and then from 370 to 320mm in diameter, as shown in Figure 4. This idealized electrode profile is used in the simulations instead of the actual experimental geometry. A key indicator for comparing the two different side arcing scenarios (25 and 30 pct) is the pool depth during ingot growth, as shown in Figure 4. For each side arcing scenario, the pool depth is represented by liquid fractions of 0.97 and 0.06.

In the initial simulation stage (from 250 up to 900mm), as shown in Figure 4, where experimental melt rate data were not available, a constant melt rate was assumed. As the ingot height increased from 250 to 500mm, the pool depth also increased. Beyond 500, up to 900mm of ingot height, the pool depth remained nearly constant, with only slight increases. Once the

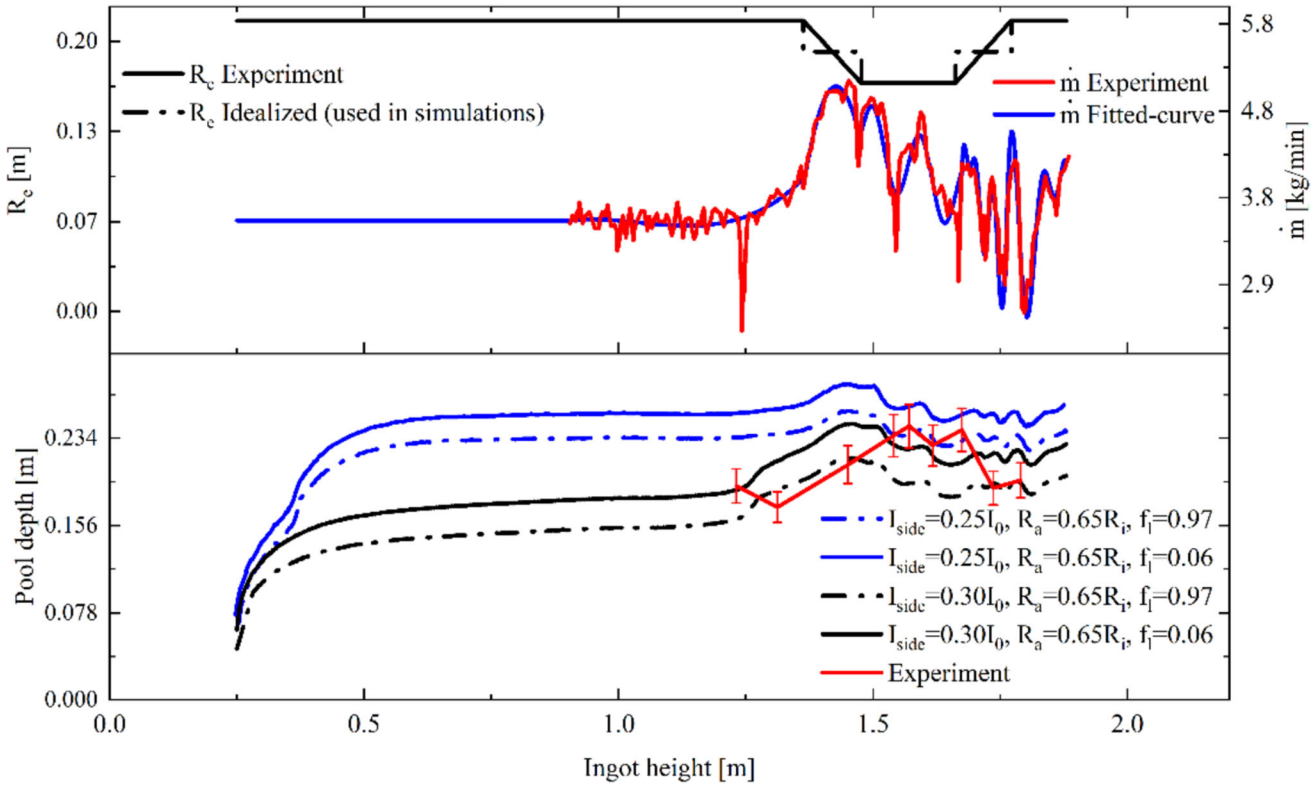

Fig. 4—(Top) Melting rate and electrode diameter variation for experiment and simulation. (Bottom) Pool depth for 25 and 30 pct side arcing with a 65 pct arc ratio, compared to the experiment.

height exceeded one meter, where the melt rate began to vary, the pool depth also started to change. As the melt rate increased, the pool depth deepened accordingly. After reaching an ingot height of 1360mm, the first reduction in electrode diameter occurs (from 420 to 370mm). A smaller electrode diameter means the current is concentrated over a smaller area, which increases both the melt rate and the pool depth, as shown in Figure 4. However, at the smallest diameter, a decrease in the melt rate is observed, which also leads to a corresponding decrease in pool depth. When the diameter is increased again (from 310 to 370mm), the melt rate fluctuates but generally shows a decreasing trend. To fully understand these fluctuations throughout the process, detailed information on the arc distribution is required, which was not available in the conducted experiment.[19]

From the comparison of the simulation results of two different side arcing scenarios, as shown in Figure 4, it is evident that an increase in side arcing results in a decrease in pool depth. This implies that less current is passing through the ingot, leading to a reduction in the arc intensity and Lorentz forces at the top of the ingot. Consequently, the pool depth diminishes. It is also notable that a 5 pct increase in side arcing results in approximately 80*mm* decrease in pool depth for this alloy, indicating high sensitivity to arc distribution.

The graph, in Figure 4, not only compares the two different side arcing scenarios but also includes experimental data on pool depth from Wang *et al.*[19] As the electrode diameter decreases, causing the melt rate to increase, the pool depth increases. Conversely, when the electrode diameter increases back to its initial size (from 370 to 420mm), the pool depth decreases. This trend is reflected in the simulation results, which show an initial increase in pool depth followed by a decrease, aligning with experimental observations, as shown in Figure 4. Additionally, the experimental pool depth falls within the range of 25 pct to 30 pct side arcing in the simulations. In the final phase of the experiment (1700 to 1750mm), a sharp decrease in the pool depth was observed, which cannot be fully explained by side arcing alone, this discrepancy between experimental results and simulation outcomes suggests that additional factors, such as variations in arc distribution, may influence pool depth, as will be described in Section III-B.

While the experimental melt rate in Figure 4 (Top) shows sharp early fluctuations before the onset of electrode diameter changes, these initial variations were not included in the simulation input.

Figure 5(a) shows the melt pool profile obtained from the experiments conducted by Wang *et al.*[19] The experimental pool depth curve was reconstructed from discrete etched cross-sections of the ingot, as reported in their study. While various methods exist for determining melt pool profiles, such as adding tracer particles to the pool and later identifying them in cross-sections, the etched cross-section method is more common but generally less precise, leading to some measurement uncertainty. For this reason, an error margin was included by Wang *et al.*[19] with the experimental pool

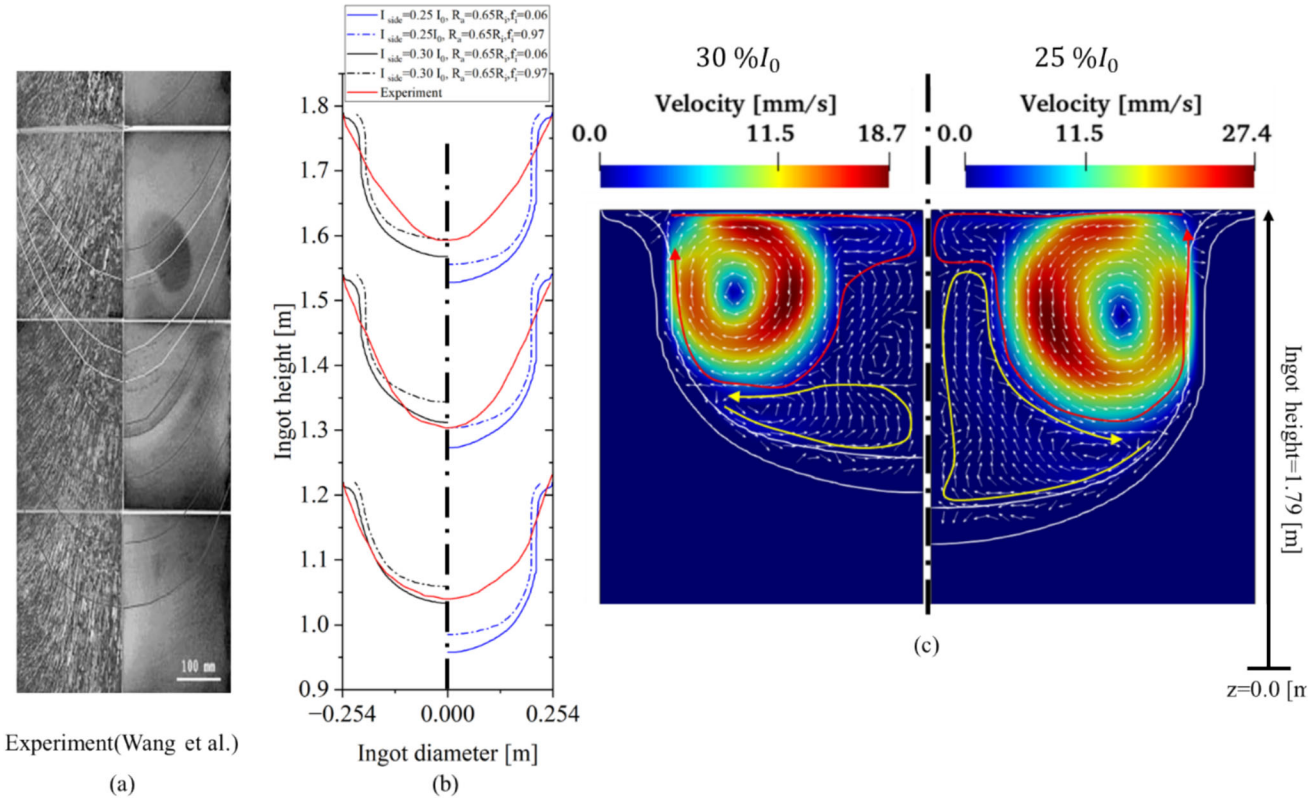

Fig. 5—(*a*) Experimental pool profiles from Metallurgical and Materials Transactions A,[19] the pool depth curve was reconstructed from discrete etched cross-sections of the ingot, as reported in the same study. (*b*) Melt pool profiles at three ingot heights for side arcing values of 30 pct (black, left) and 25 pct (blue, right), compared to experimental data (red) at a fixed arc ratio of 65 pct. (*c*) Velocity contours in the melt pool for the same side arcing and arc ratio values as in (b) with white vectors indicating flow direction only and are not scaled by velocity magnitude. Liquid fraction isolines of 0.06 and 0.97. The red and yellow arrows represent the EVF and TBF, respectively (Color figure online).

depth data. Figure 5(b) compares the melt pool profiles at three ingot heights for two side arcing values: 30 pct (black curve, left) and 25 pct (blue curve, right), with a fixed arc ratio of 65 pct.

The case with 30 pct side arcing closely aligns with the experimental data,[19] especially in the lower section pool profiles, as shown in Figure 5(b), along the ingot height. As the ingot builds up, the experimental pool profile becomes narrower compared to the simulation, likely due to variations in arc behavior or differences in the gas cooling heat transfer coefficient. However, without experimental data of the detailed arc distribution, it is difficult to forecast which parameter is responsible for this discrepancy. In contrast, the case with 25 pct side arcing results in a deeper pool profile at various ingot heights, while the middle-section pool profile, as shown in Figure 5(b), closely matches the experimental data. Comparing these simulation cases with the experimental results suggests that the possible side arcing value for the middle-section pool profile is likely between 25 and 30 pct, as the experimental data fall within this range.

Figure 5(c) presents velocity contours for side arcing values of 30 pct (left) and 25 pct (right) with a fixed arc ratio of 65 pct.

In the melt pool, the red arrow represents the EVF created by the Lorentz force, while the yellow arrow indicates the TBF generated by the thermal gradient, which is significantly weaker than the EVF in both cases. The EVF predominates in the pool area, generating a strong vortex near the ingot's outer surface beneath the electrode, which leaves minimal space for the TBF. Reducing side arcing by 5 pct allows more current through the ingot, resulting in a roughly 45 pct increase in velocity and a more pronounced EVF.

B. *Effects of Arc Distribution*

The impact of arc distribution on transient ingot pool depth in VAR is shown in Figure 6, both with 30 pct side arcing but different arc ratios of 65 pct and 70 pct. The simulated pool depth shows that reducing the arc ratio results in a shallower pool, with a consistent 20mm difference between the two arc ratios while the electrode radius remains constant. However, once the electrode radius changes, the pool depth difference increases significantly to 50mm. At ingot heights between 1250 and 1500mm, the experimental pool depth is overestimated compared to the 65 pct arc ratio simulation and underestimated with the 70 pct arc ratio, suggesting the

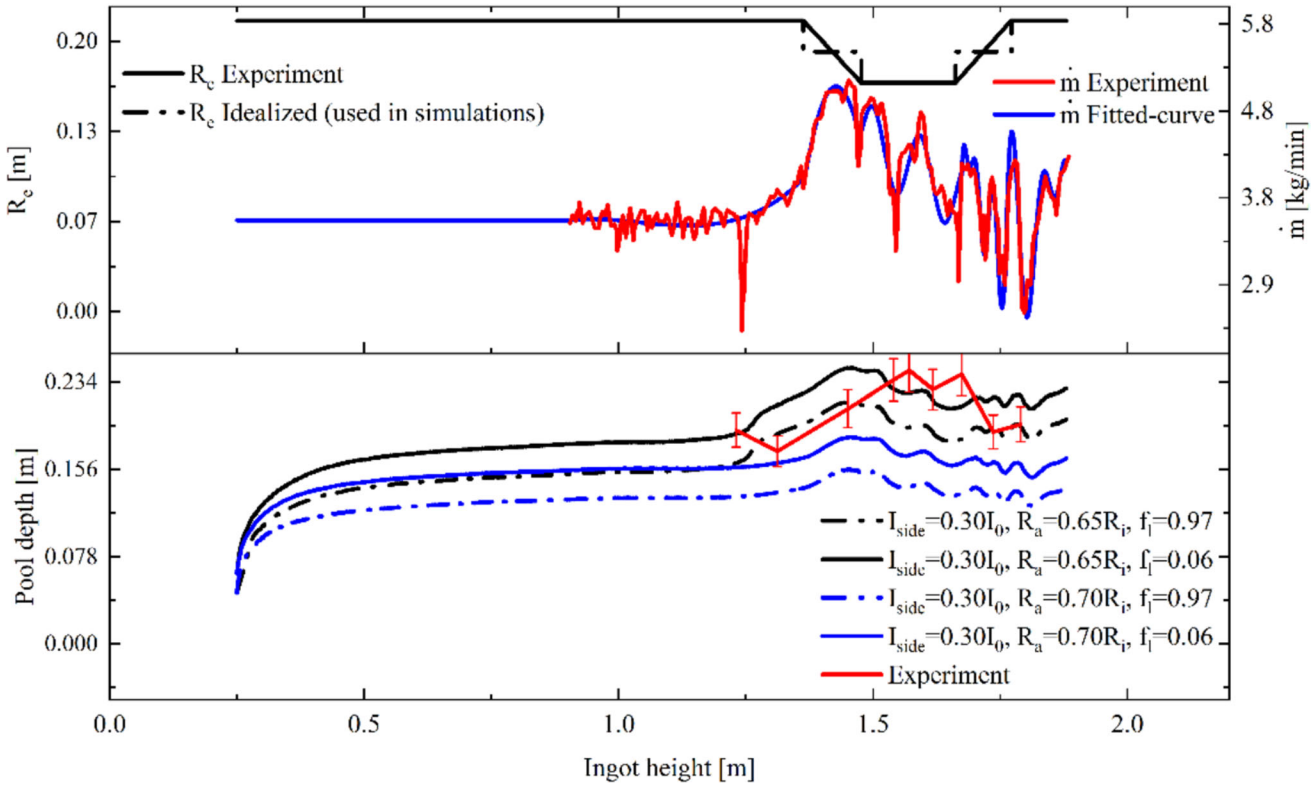

Fig. 6—(Top) Variation in melting rate and electrode diameter for both the experiment and simulation. (Bottom) Pool depth for cases with arc ratios of 65 pct and 75 pct, with a side arcing of 30 pct for both, including the pool depth reported in the experiment.

actual arc ratio lies between these values. From 1500 to 1750mm, both simulations underestimate the pool depth, indicating a more constricted arc as the electrode diameter decreases. This implies that the arc ratio is around 60 pct at this stage.

Figure 7(a) repeats the experimental pool profile as the Reference 19. Figure 7(b) shows melt pool profiles at three different ingot heights for two arc ratios of 65 pct(*left*) and 70 pct(*right*), where a side arcing value is fixed to 30 pct. The pool depth is underestimated at all reported pool profiles with a 70 pct arc ratio, with the largest discrepancy in the middle-section pool profile, as shown in Figure 7(b). This suggests that the arc ratio should be reduced across all pool profiles, with greater constriction needed specifically for the middle-section pool profile, where the electrode size decreased. Figure 7(c) shows the velocity distribution for two cases: the 65 pct arc ratio (left) and the more diffuse 70 pct arc ratio (right). A higher arc ratio promotes a more uniform spread of electric arc and heat across the ingot surface, weakening the EVF (red arrow) and drawing less hot fluid from the top surface, resulting in a shallower melt pool. In the 70 pct arc ratio case, the TBF (yellow arrow) becomes stronger and occupies about half of the melt pool, while in the 65 pct case, the EVF dominates.

This implies that a slight increase (5 pct) in arc ratio significantly reduces the EVF's maximum velocity by roughly 40 pct.

This study highlights the importance of arc distribution parameters, particularly side arcing and arc ratio, in influencing the dynamics of the melt pool during vacuum arc remelting (VAR) throughout the transient growth of the ingot from initiation to completion. The findings emphasize the need for further investigation into optimal arc distributions and side arcing concerning varying electrode diameters, melt rate, electric current, and the evolving height of the ingot.

C. *Effects of Joule Heating*

To validate the assumption of neglecting Joule heating in our primary simulations, we performed an additional case study comparing two scenarios: one with Joule heating ($\frac{J_r^2+J_z^2}{\sigma}$) and one without. The comparison focused on the temperature distribution and melt pool depth during ingot growth under identical boundary conditions. As shown in Figure 8(a), the temperature distribution and pool profile exhibit almost no difference between the two cases at two different ingot heights. Figure 8(b) presents the Joule heating distribution across the domain at two growth stages. Furthermore,

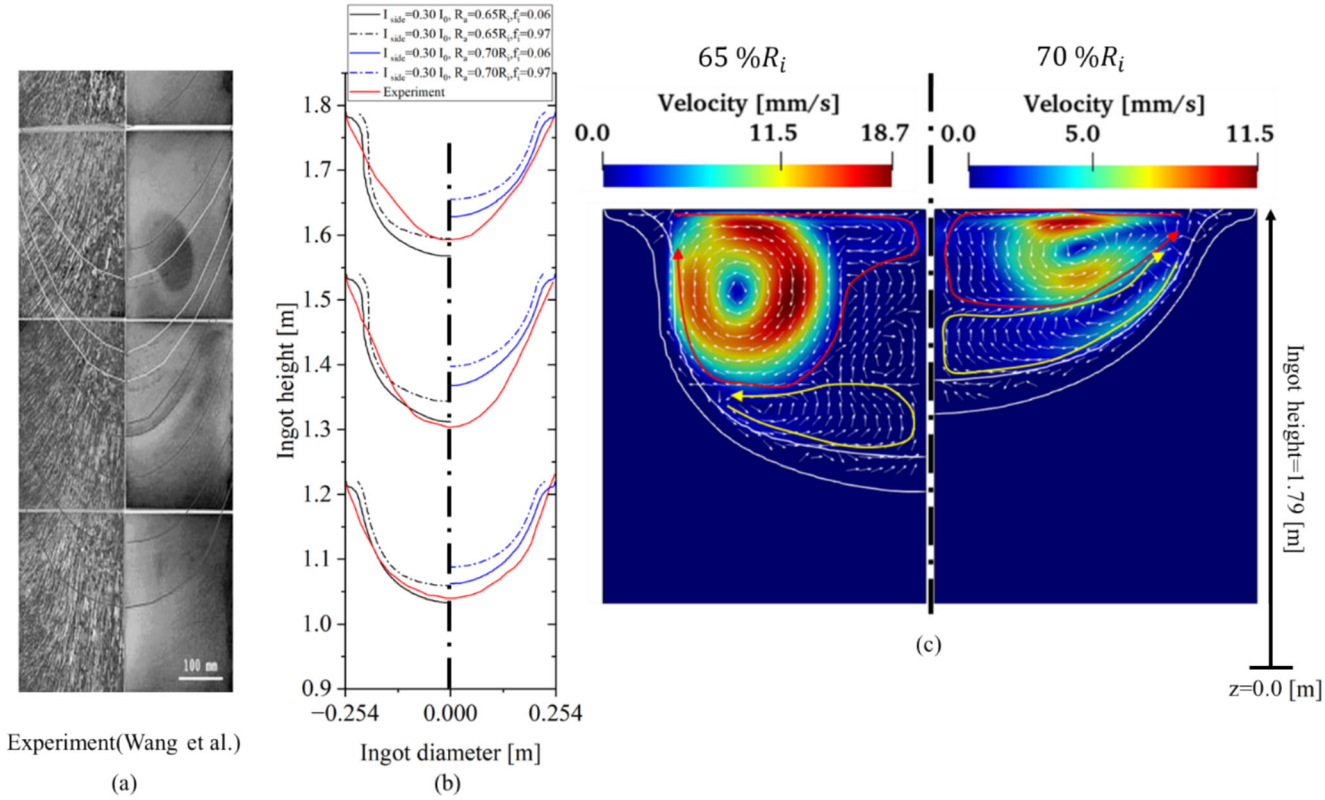

Fig. 7—(*a*) Experimental pool profiles from Metallurgical and Materials Transactions A,[19] the pool depth curve was reconstructed from discrete etched cross-sections of the ingot, as reported in the same study. (*b*) Melt pool profiles at three ingot heights for arc ratio values of 65 pct (black, left) and 70 pct (blue, right), compared to experimental data (red) at a fixed side arcing of 30 pct. (*c*) Velocity contours in the melt pool for the same arc ratio values, with white vectors indicating flow direction only and are not scaled by velocity magnitude. Liquid fraction isolines of 0.06 and 0.97. The red and yellow arrows represent the EVF and TBF, respectively (Color figure online).

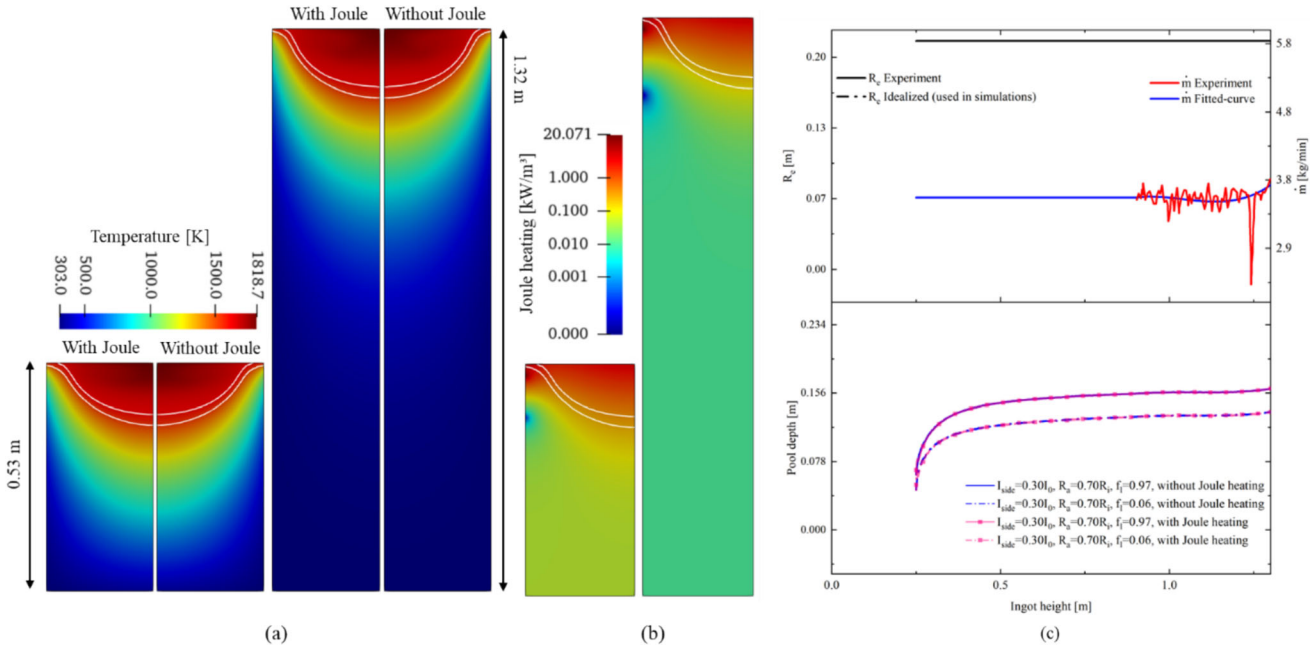

Fig. 8—(*a*) Comparison of temperature distribution and pool profile at two different ingot heights for cases with and without Joule heating for a side arcing of 30 pct and an arc ratio of 70 pct, Isolines denote liquid fractions of 0.97 and 0.06. (*b*) Joule heating distribution across the domain at two ingot growth stages. (*c*) Pool depth versus ingot height comparison, showing minimal difference between simulations with and without Joule heating.

Figure 8(c) (Ingot Height vs. Pool Depth) shows that the pool depth remains nearly identical throughout the entire process for both cases. These results confirm that Joule heating has a minimal impact on the overall energy balance, supporting its exclusion from the current modeling framework without compromising accuracy.

IV. CONCLUSIONS

In this study, a 2D axisymmetric transient model is employed to simulate the vacuum arc remelting (VAR) process, capturing the evolution of electric current density, magnetic field, Lorentz force, temperature, velocity, and liquid fraction throughout ingot growth, from the base (start stage) to the final height (feeding stage). The effects of side arcing and arc ratio on melt pool dynamics are analyzed during the transient growth of INCONEL® 718 ingots, with a focus on variations in mass flow rate and electrode diameter. Key findings include the following:

- The electro-vortex flow (EVF) is the primary factor influencing melt pool behavior, significantly impacting both pool depth and flow distribution compared to thermal buoyancy flow (TBF).
- A slight increase in side arcing (*e.g.*, 5 pct) significantly enhances the EVF, resulting in a deeper melt pool compared to a slight decrease (*e.g.*, 5 pct) in the arc ratio, specifically when the ingot pool is far from the cooling of the base plate.
- Decreasing the electrode size while maintaining a constant imposed electric current increases the melt rate over a smaller area, leading to a deeper pool profile.
- As the pool moves further from the baseplate, around one diameter of the ingot, the pool profile experiences only slight variations when both current and melt rate are kept constant, indicating achieving steady growth of the ingot.

The simulation results, including animations, validated against experimental data, provide engineers with valuable insights into the effects of significant variations in process parameters, such as melt rate and electrode diameter, within the VAR process.

CONFLICT OF INTEREST

On behalf of all authors, the corresponding author states that there is no conflict of interest.

OPEN ACCESS

SUPPLEMENTARY INFORMATION

The online version contains supplementary material available at https://doi.org/10.1007/s11663-025-03749-8.

NOMENCLATURE

A_{mush}	Mushy zone coefficient, $kgm^{-3}s^{-1}$
B_θ	Magnetic flux density in the tangential direction, T
C_0	Initial solute concentration, *wt* pct
C_p	Heat capacity, $Jkg^{-1}K^{-1}$
f_l	The volume fraction of liquid, –
f_R	Arc ratio, –
$f_{side-arc}$	Fraction of electric current as side arcing, –
F_z, F_r	Lorentz force in the axial and the radial direction, Nm^3
g	Gravitational acceleration, ms^{-2}
h	Local enthalpy, Jkg^{-1}
h_{ideal}	The height of the defined mesh size, m
h_{ingot}	Ingot height, m
h_{mesh}	The height of the new layer of mesh, m
h_{ref}	Reference enthalpy, Jkg^{-1}
i, j	Unit vectors in axial, and radial directions, –
I_0	Total imposed current, A
J_z, J_r	Electric current density in the axial and the radial direction, Am^{-2}
k_{eff}	Effective thermal conductivity, $Wkg^{-1}m^{-1}$
k	Equilibrium partition coefficient, –
I	Electric current intensity, kA
L	Latent heat of solidification, Jkg^{-1}
$\dot{m}$	Mass flow rate, $kgmin^{-1}$
m_l	Slope of the liquidus line, $k\,pct^{-1}$
p	Pressure, Nm^{-2}
R_a	Radius of arc, m
R_e	Radius of electrode, m
R_i	Radius of ingot, m
R_m	Radius of mold, m
S_h	Enthalpy source term, $Jm^{-3}s^{-1}$
S_{u_z}, S_{u_r}	Axial and radial velocity source term, Nm^{-3}
T	Temperature, K
T_l	Liquidus temperature, K
T_m	Melting temperature, K
T_s	Solidus temperature, K
u_{mesh}	Velocity of dynamic mesh, ms^{-1}
u_z, u_r	Axial and radial velocity, ms^{-1}

z, r	Coordinate in the axial and the radial direction of the ingot, m
α_c	Split factor, m
β	Thermal expansion, K^{-1}
κ	Permeability, m^2
λ_1	Primary dendrite arm spacing, m
σ_e	Electric conductivity, $\Omega^{-1}m^{-1}$
μ_{eff}	Effective viscosity, Pas
μ_m	The magnetic permeability, $Jm^{-1}A^{-2}$
ρ	Density, kgm^{-3}
ϕ	Electrical potential, V

REFERENCES

1. M. Abdi, E. Karimi-Sibaki, C. Sommitsch, H. Barati, M. Al--Nasser, M. Wu, I. Teplyakov, and A. Kharicha: *Int. J. Thermofluids*, 2024, vol. 23, p. 100721.
2. A. Mitchell: *Mater. Sci. Eng. A*, 2005, vol. 413–414A, pp. 10–18.
3. L. Bertram: *Modeling for casting and solidification processing*, Marcel Dekker, Inc, New York, 2002, pp. 565–612.
4. I.I. Beilis: *IEEE Trans. Plasma Sci.*, 2019, vol. 47, pp. 3412–33.
5. J.M. Lafferty: *Encyclopedia of physical science and technology*, Elsevier, Amaterdam, 2003, pp. 359–70.
6. B. Juttner: *IEEE Trans. Plasma Sci.*, 1987, vol. 15, pp. 474–80.
7. A. Anders, S. Anders, B. Jüttner, H. Pursch, W. Bötticher, and H. Lück: *J. Appl. Phys.*, 1992, vol. 71, pp. 4763–70.
8. R.L. Boxman, D.M. Sanders, and P.J. Martin, eds.: *Handbook of vacuum arc science and technology: fundamentals and applications*, Noyes Publications, Park Ridge, 1995.
9. A. Anders: *Cathodic arcs: from fractal spots to energetic condensation*, Springer, New York, 2008.
10. B. Tezenas Du Montcel, P. Chapelle, C. Creusot, and A. Jardy: *IEEE Trans. Plasma Sci.*, 2018, vol. 46, pp. 3722–30.
11. A.M. Chaly, A.A. Logatchev, and S.M. Shkol'nik: *IEEE Trans. Plasma Sci.*, 1997, vol. 25, pp. 564–70.
12. Z. Zalucki and J. Janiszewski: *IEEE Trans. Plasma Sci.*, 1999, vol. 27, pp. 991–1000.
13. L.G. Hosamani: Oregon Health & Science University, 1988.
14. J.M. Wentzell: US patent US3353585A, 1967, p. 2.
15. L.G. Hosamani, W.E. Wood, and J.H. Devletian: *Superalloys 718 metallurgy and applications (1989)*, TMS, Pittsburgh, 1989, pp. 49–57.
16. E. Karimi-Sibaki, A. Kharicha, M. Wu, A. Ludwig, and J. Bohacek: *Metall. Mater. Trans. B*, 2020, vol. 51B, pp. 222–35.
17. J. Bohacek, E. Karimi-Sibaki, A. Vakhrushev, K. Mraz, J. Hvozda, M. Wu, and A. Kharicha: *Metall. Mater. Trans. B*, 2024, vol. 55B, pp. 4408–17.
18. M. Sankar, V.V. Satya Prasad, R.G. Baligidad, and A.A. Gokhale: *Int. J. Refract. Metals Hard Mater.*, 2015, vol. 50, pp. 120–25.
19. X. Wang, R.M. Ward, M.H. Jacobs, and M.D. Barratt: *Metall. Mater. Trans. A*, 2008, vol. 39A, pp. 2981–89.
20. G. Shayesteh, A. Ludwig, M. Stefan-Kharicha, M. Wu, and A. Kharicha: *J. Phys. Conf. Ser.*, 2024, vol. 2766, p. 012199.
21. K. Pericleous, G. Djambazov, M. Ward, L. Yuan, and P.D. Lee: *Metall. Mater. Trans. A*, 2013, vol. 44A, pp. 5365–76.
22. D. Jiang and L. Zhang: *JOM*, 2023, vol. 75, pp. 1505–14.
23. A. Kermanpur, D.G. Evans, R.J. Siddall, P.D. Lee, and M. McLean: *J. Mater. Sci.*, 2004, vol. 39, pp. 7175–82.
24. R.L. Williamson, J.J. Beaman, D.K. Melgaard, G.J. Shelmidine, A.D. Patel, and C.B. Adasczik: *J. Mater. Sci.*, 2004, vol. 39, pp. 7161–68.
25. R.L. Williamson, D.K. Melgaard, G.J. Shelmidine, J.J. Beaman, and R. Morrison: *Metall. Mater. Trans. B*, 2004, vol. 35B, pp. 101–13.
26. J. Cui, B. Li, Z. Liu, Y. Xiong, F. Qi, Z. Zhao, and S. Zhu: *Metall. Mater. Trans. B*, 2023, vol. 54B, pp. 661–72.
27. P.-O. Delzant, B. Baqué, P. Chapelle, and A. Jardy: *Metall. Mater. Trans. B*, 2018, vol. 49B, pp. 958–68.
28. D. Jiang, Y. Ren, and L. Zhang: *JOM*, 2024, vol. 76, pp. 3362–71.
29. ANSYS, Inc.: ANSYS Fluent, Release, 2017. ANSYS, Inc.
30. R.L. Williamson, G.J. Shelmidine, and J.P. Maroone: in Report Number: SAND2005-2838C, Research Org.: Sandia National Laboratories (SNL), Albuquerque, NM, and Livermore, 2005.
31. P.D. Lee, R. Lothian, L.J. Hobbs, and M. McLean: in Superalloys 1996 (Eighth International Symposium), TMS, 1996, pp. 435–42.
32. D. Zagrebelnyy and M.J.M. Krane: *Metall. Mater. Trans. B*, 2009, vol. 40B, pp. 281–88.
33. J.J. Beaman, L. Felipe Lopez, and R.L. Williamson: *J. Dyn. Syst. Meas. Control*, 2014, vol. 136, p. 031007.
34. E. Karimi-Sibaki, A. Kharicha, M. Abdi, A. Vakhrushev, M. Wu, A. Ludwig, and J. Bohacek: *Metall. Mater. Trans. B*, 2021, vol. 52B, pp. 3354–62.
35. L. Yuan, G. Djambazov, P.D. Lee, and K. Pericleous: *Int. J. Mod. Phys. B*, 2009, vol. 23B, pp. 1584–90.
36. C.R. Woodside, P.E. King, and C. Nordlund: *Metall Materi Trans B*, 2013, vol. 44B, pp. 154–65.
37. E. Karimi-Sibaki, A. Kharicha, A. Vakhrushev, M. Abdi, M. Wu, A. Ludwig, J. Bohacek, and B. Preiss: *J. Market. Res.*, 2022, vol. 19, pp. 183–93.
38. S. Spitans, H. Franz, H. Scholz, G. Reiter, and E. Baake: *Magnetohydrodynamics*, 2017, vol. 53, pp. 557–69.
39. X. Xu, W. Zhang, and P.D. Lee: *Metall. Mater. Trans. A*, 2002, vol. 33A, pp. 1805–15.
40. E. Scheil: *Int. J. Mater. Res.*, 1942, vol. 34, pp. 70–72.
41. M.C. Schneider, J.P. Gu, C. Beckermann, W.J. Boettinger, and U.R. Kattner: *Metall. Mater. Trans. A*, 1997, vol. 28A, pp. 1517–31.
42. P.A. Davidson, X. He, and A.J. Lowe: *Mater. Sci. Technol.*, 2000, vol. 16, pp. 699–711.
43. E.N. Kondrashov, A.Y. Maksimov, and L.V. Konovalov: *Russ. J. Non-ferrous Metals*, 2008, vol. 49, pp. 23–27.
44. E.N. Kondrashov, M.I. Musatov, A.Y. Maksimov, A.E. Goncharov, and L.V. Konovalov: 2005.
45. M.C. Schneider and C. Beckermann: *Int. J. Heat Mass Transf.*, 1995, vol. 38, pp. 3455–73.
46. P.C. Carman: *Chem. Eng. Res. Des.*, 1997, vol. 75, pp. S32–48.
47. V.R. Voller and C. Prakash: *Int. J. Heat Mass Transf.*, 1987, vol. 30, pp. 1709–19.
48. F.R. Menter: *AIAA J.*, 1994, vol. 32, pp. 1598–1605.
49. A.S. Agazhanov, D.A. Samoshkin, and Y.M. Kozlovskii: *J. Phys. Conf. Ser.*, 2019, vol. 1382, p. 012175.
50. K. Jin, Z. Yang, P. Chen, G. Huang, and X. Qiao: *Int. J. Heat Mass Transf.*, 2022, vol. 192, p. 122907.
51. P. Nie, O.A. Ojo, and Z. Li: *Acta Mater.*, 2014, vol. 77, pp. 85–95.
52. Z. Jin, X. Kong, L. Ma, J. Dong, and X. Li: *Materials*, 2023, vol. 16, p. 3479.
53. W. Xiao, S. Li, C. Wang, Y. Shi, J. Mazumder, H. Xing, and L. Song: *Mater. Des.*, 2019, vol. 164, p. 107553.
54. H. Hosaeus, A. Seifter, E. Kaschnitz, and G. Pottlacher: *High Temp. High Press.*, 2001, vol. 33, pp. 405–10.
55. A. Risacher, P. Chapelle, A. Jardy, J. Escaffre, and H. Poisson: *J. Mater. Process. Technol.*, 2013, vol. 213, pp. 291–99.
56. R.M. Ward and M.H. Jacobs: *J. Mater. Sci.*, 2004, vol. 39, pp. 7135–43.
57. C.R. Woodside and P.E. King: *TMS Annual Meeting*, 2009, pp. 75–84.
58. C.R. Woodside and P.E. King: *IEEE Instrum. Meas. Technol. Conf. Proc.*, 2010, vol. 2010, pp. 452–57.
59. P.-O. Delzant, P. Chapelle, A. Jardy, J. Jourdan, J. Jourdan, and Y. Millet: *J. Mater. Process. Technol.*, 2019, vol. 266, pp. 10–18.
60. M. Cibula, R. Woodside, P. King, and G. Alanko: 2017.
61. P.-O. Delzant, P. Chapelle, A. Jardy, A. Matveichev, and Y. Millet: *Metals*, 2022, vol. 12, p. 500.
62. R.M.A. Jr and R.L. Williamson: *TMS (The Minerals, Metals and Materials Society)*, 2009, pp. 65–74.
63. B.G. Nair, N. Winter, B. Daniel, and R.M. Ward: *IOP Conf. Ser. Mater. Sci. Eng.*, 2016, vol. 143, p. 1012012.
64. F. Zanner, R. Williamson, and R. Erdmann: *LMPC*, 2005, pp. 13–27.
65. R.M. Ward, B. Daniel, and R.J. Siddall: *LMPC*, 2005, pp. 49–56.
66. F.J. Zanner: San Diego, 1979, pp. 417–26.
67. M. Cibula, P. King, and J. Motley: *Metall. Mater. Trans. B*, 2020, vol. 51B, pp. 2483–91.

68. E. Karimi-Sibaki, M. Peyha, A. Vakhrushev, M. Wu, A. Ludwig, J. Bohacek, B. Preiss, and A. Kharicha: *Sci. Rep*., 2022, vol. 12, p. 20405.
69. P. Chapelle, C. Noël, A. Risacher, J. Jourdan, A. Jardy, and J. Jourdan: *J. Mater. Process. Technol*., 2014, vol. 214, pp. 2268–75.
70. R.L. Williamson and G.J. Shelmidine: in *Superalloys 718, 625, 706 and Various Derivatives (2001)*, TMS, 2001, pp. 91–102.
71. P. Chapelle, R.M. Ward, A. Jardy, V. Weber, J.P. Bellot, and M. Minvielle: *Metall. Mater. Trans. B*, 2009, vol. 40, pp. 254–62.